NJC

ROYAL SOCIETY OF CHEMISTRY

PAPER

View Article Online
View Journal | View Issue

Cite this: *New J. Chem.*, 2024, **48**, 14736

Preparation and characterization of conductive and multi-network nanocomposite hydrogels as potential scaffolds for electroactive tissues

Rumeysa Tutar, *[a] Deniz Ceylan [b] and Betül Çelebi-Saltik[c]

Electroactive scaffolds are increasingly used to mimic the microenvironment of electroactive tissues such as the heart and nerves. Multi-network hydrogels have emerged as an important platform in the field of tissue engineering. In this study, alginate (Alg)-based conductive and multi-network nanocomposite hydrogels were prepared and characterized as promising scaffolds for electroactive tissues. Alg, which is derived from natural sources, was modified with methacrylate (AlgMA) to render it photosensitive (photoactive). Multiwall carbon nanotubes (MWCNTs) were chosen as potential nanomaterials for electrical conductivity. MWCNTs were modified with –COOH groups to produce MWCNT–COOH nanomaterials. Nanocomposite hydrogels were fabricated by incorporating 0.5%, 1.0%, and 3.0 wt% of MWCNT–COOH into the AlgMA network. The hydrogel scaffolds were assessed for their chemical, physical, mechanical, electrical, and biological characteristics. This study demonstrated that incorporating modified MWCNTs into an AlgMA network enhances its electrical activity. According to our results, good rheological properties, natural tissue-like mechanical properties, optimal electrical conductivity, and biological performance make AlgMA/MWCNT–COOH multi-network nanocomposite hydrogels crucial in the field of electroactive tissues.

Received 26th April 2024,
Accepted 26th July 2024

DOI: 10.1039/d4nj01930j

rsc.li/njc

Introduction

Electroactive scaffold structures are increasingly being employed to mimic the microenvironment of electroactive tissues such as the heart and nerves. Heart disease is one of the leading causes of death and disability worldwide. The utilization of biocompatible and biomimetic extracellular matrices (ECMs) such as alginate, which can substitute damaged heart tissues, is a crucial focus in cardiac tissue engineering applications. However, the existing systems porous notable challenges. Specifically, the pore walls of macroporous structures diminish the electrical conductivity.[1,2]

Alginates are linear polysaccharides derived from seaweed and bacteria.[3] Ionic crosslinking with divalent cations is commonly used to produce alginate-based hydrogels. However, this crosslinking mechanism is not suitable for preparing and controlling robust alginate-based hydrogels.[4] Because of this fragility, modification methods are applied to make alginate hydrogels more stable and robust in terms of physical and mechanical properties. In this study, methacrylated modified alginate (AlgMA) was prepared to make alginate hydrogels dual-crosslinked with visible light and divalent cations (Ca^{2+}).[5] Different strategies have been developed to enhance various properties of alginate hydrogels, especially their mechanical strength. Although one of the most common methods for improving network structures is dual crosslinking, the addition of nanomaterials to the network environment also positively affects the mechanical properties.[6]

Carbon-based nanomaterials have been used in various fields, especially in biomedical applications such as tissue engineering. Especially, graphene and carbon nanotubes (CNTs) have exceptional physical and chemical properties such as electrical conductivity, thermal stability, and mechanical strength[2] (exceptionally high tensile strength and stiffness).[7,8] In addition, CNTs have incredibly strong properties due to their flexibility and stretchability.[9] However, the surface of multi-walled carbon nanotubes (MWNTs) is inert, and this property reduces their potential applications. Additionally, they are hydrophobic. Therefore, the oxidation of MWCNTs can be applied to enhance the chemical reactivity.[10] Nanocomposite hydrogels have received significant attention in tissue engineering applications. For instance, in a study, aligned CNTs were successfully incorporated into flexible and biocompatible hydrogels, demonstrating excellent anisotropic electrical conductivity. Bioactuators were engineered by culturing cardiomyocytes on a CNT microelectrode-integrated

[a] *Department of Chemistry, Faculty of Engineering, Istanbul University-Cerrahpaşa, Avcılar, Istanbul, 34320, Turkey. E-mail: rumeysa.tutar@iuc.edu.tr*
[b] *Bezmialem Vakif University, Faculty of Pharmacy, Istanbul 34093, Turkey*
[c] *Department of Stem Cell Sciences, Hacettepe University Graduate School of Health Sciences, Center for Stem Cell Research and Development, Ankara, 06100, Turkey*

hydrogel construct. The centimeter-scale bioactuator fabricated in their study exhibited excellent mechanical integrity, embedded microelectrodes, and the capability for spontaneous actuation behavior.[11] It clearly elaborates on the relationship between electroactive and related bio-applications.

Some studies on double-network (DN) system-based conductive nanocomposite hydrogels have been discussed. In one study, polyvinyl alcohol-borate (PVA-Borax)/CNT based double-network conductive hydrogels were developed for wearable sensors. Here, iron(III)–thioctic acid (TA) was selected as coordination materials to improve the self-healing ability.[12] In another study, polyacrylamide/sodium alginate/carbon nanotube (PAAm/SA/CNT) double-network (DN) hydrogels were prepared for use in remote actuation and low-temperature strain sensing applications. Calcium chloride ($CaCl_2$) was used as an ionic crosslinker for SA.[13] Moreover, in a different study, robust, conductive double-network hydrogels based on polyacrylamide (PAM) polymers with well-dispersed carbon nanotubes were developed for advanced force sensing applications.[14]

Various types of bonds are used to create multi-network structures, and the molecular strength of these bonds plays an active role in creating the structure. In this study, multi-network structures were obtained through various intra- and intermolecular bonds. Methacrylate-modified alginate is covalently cross-linked within its structure by visible light, and ionically cross-linked by creating electrical bonds in the presence of Ca^{2+} ions. The COOH-modified MWCNTs and AlgMA formed hydrogen bonds between molecules.

The main aim of this study was to demonstrate that AlgMA/MWCNT–COOH nanocomposite hydrogels can be used in electroactive tissue engineering applications. Modified MWCNTs were obtained by surface modification of pristine MWCNTs. Nanocomposite hydrogels were fabricated by incorporating 0.5%, 1.0%, and 3.0 wt% of MWCNT–COOH into multi-network AlgMA using a magnetic stirrer. The eosin Y, *N*-vinylcaprolactam (VC)/triethanolamine (TEA) photoinitiator system was first covalently crosslinked to nanocomposite hydrogels under visible curing light (VALO). In addition, for dual-crosslinking, 1 M Ca^{2+} ions were used for ionic crosslinking to achieve more stable nanocomposite hydrogels with good mechanical properties, low degradation rate, good rheological performance, and good electrical conductivity. The prepared modified Alg, MWCNTs, and nanocomposite hydrogels were characterized using different spectroscopic methods, such as Fourier transform infrared (FTIR) and nuclear magnetic resonance (NMR) spectroscopy, and microscopic methods, such as scanning electron microscopy (SEM) and transmission electron microscopy (TEM). Moreover, the influence of MWCNT content on the biological properties was examined using cell experiments.

Results and discussion

Characterization studies

Pristine alginate (Alg) and methacrylate-functionalized alginate (AlgMA) were characterized using FTIR and ^{1}H-NMR spectroscopy to evaluate their chemical structures. Fig. 1 shows the

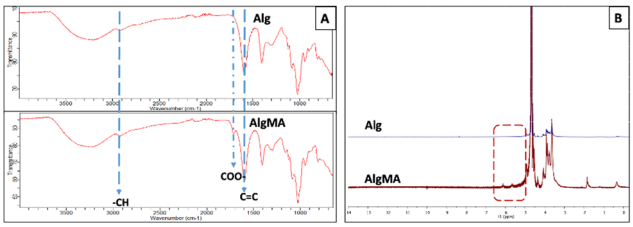

Fig. 1 (A) FTIR, (B) NMR characterization of Alg and AlgMA.

FTIR and NMR characterization of the synthesized macromers under the optimized conditions.

The FTIR spectra of all the studied samples were recorded between 4000 and 500 cm^{-1} using a Jasco FT/IR 6700 spectrophotometer (Fig. 1(A)). Regions 3700–3000 and 2980–2850 cm^{-1} correspond to the stretching of the –OH and –CH groups, respectively.[15] The bands marked with blue arrows show aliphatic chains (2980–2850 cm^{-1}), C=C aromatic structures (1600 cm^{-1}), and carboxyl esters (1702 cm^{-1}) of the grafted methacrylic anhydride groups. The growth of carboxylate anion (COO–) stretching bands, which were observed in the AlgMA spectrum, showed a shoulder appearing at around 1702 cm^{-1} (shown by blue arrows).[15–17] When compared with the Alg spectrum, a band at 1702 cm^{-1} was not observed. It also shows the presence of C=C aromatic structures at 1600 cm^{-1}. The shoulder visible on the prepared AlgMA monomer shows stretching vibrations of aliphatic chains (–CH) and esters (C=O) resulting from the reaction of methacrylate units on Alg. Within the scope of these results, we observed that Alg was successfully functionalized with methacrylate anhydride.

The ^{1}H-NMR spectra of Alg and AlgMA macromers are shown in Fig. 1(B). The characteristic peaks of the saccharide units of the Alg backbone between 3.50 and 5.20 ppm were observed in the NMR spectrum. In the chemical structure formed after methacrylation, distinctive signals of ~2 ppm of groups reacting with methacrylate and vinyl groups, 5.20–6.30 ppm, and methyl hydrogens were observed in the spectrum. The signals related to the vinyl hydrogens of the groups appeared at 5.27 and 5.58 ppm for AlgMA. The signal for the methyl hydrogens of methacrylate appears as a well-defined singlet at ~1.80 ppm for the macromers.[17]

MWCNTs were functionalized with concentrated HNO_3 to enhance their reactivity with AlgMA. The native and COOH-functionalized MWCNTs were characterized by FTIR spectroscopy to evaluate their chemical structures. Fig. 2(A) and (B) show the FTIR characterization of the pristine MWCNTs and the –COOH modified MWCNTs under the optimized conditions.

The surface functional groups and chemical bonds of the MWCNTs and MWCNT–COOH structures were examined using FTIR spectroscopy. The characterization of carboxyl-functionalized carbon nanotubes included the evaluation of the –OH stretching vibration band in the range from 3700 cm^{-1} to 3500 cm^{-1}.[18,19] Pristine MWCNTs show very low intensity at around ~3600 cm^{-1} related to –OH stretching vibration. The water molecules on the carbon in the CNTs are related to the –OH peak. The band at ~1300–1400 cm^{-1} shows that the C–O

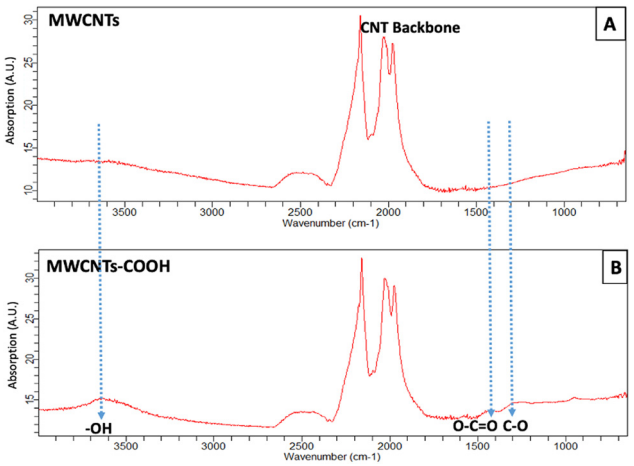

Fig. 2 FTIR characterization of (A) MWCNTs and (B) MWCNT–COOH.

and –O–C═O stretching vibrations of MWCNT were weakened, and the peak position of MWCNT–COOH deviated. This displacement was due to the substitution of oxygen-containing functional groups to break the C–C bond. The introduction of –COOH on the surface of the MWCNT was confirmed during the strong-acid treatment. In summary, MWCNTs resulted in a significant change in the FTIR spectral intensity after chemical modification, proving the successful synthesis of MWCNT–COOH.[10,20,21]

The modified MWCNTs were characterized using scanning electron microscopy (SEM) and transmission electron microscopy (TEM). TEM was employed to investigate the internal and surface microstructures of both the MWCNT and MWCNT–COOH. The TEM images of the untreated MWCNTs in Fig. 3(A) demonstrate agglomeration, which is consistent with the SEM findings in Fig. 3(C), indicating no functional group modification.

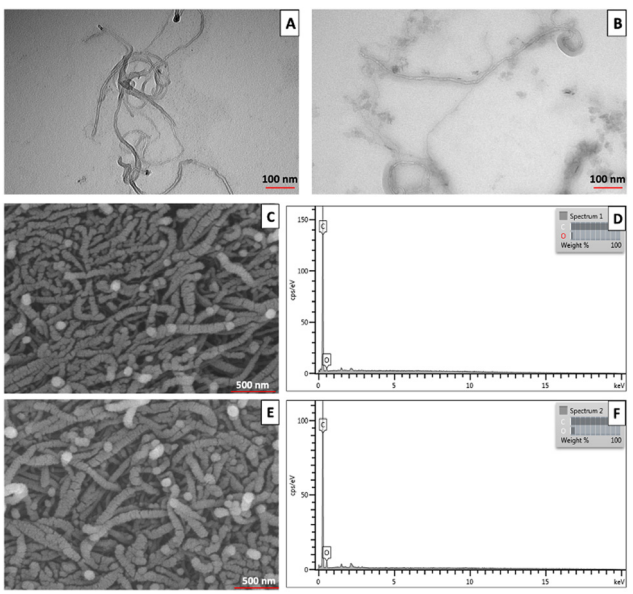

Fig. 3 TEM characterization of (A) MWCNTs, (B) MWCNT–COOH and SEM and EDS analysis of (C and D) MWCNTs, (E and F) MWCNT–COOH.

Conversely, the TEM images of MWCNT–COOH (Fig. 3(B)) revealed increased tip and length. Furthermore, the tubular structure of MWCNT–COOH transitioned into a paper sheet structure, offering more active sites for grafting–COOH groups.[19,22]

The microstructures of the MWCNT before and after functional group modification are shown in Fig. 3(C)–(E), as observed in the SEM images. In Fig. 3(C), the SEM image revealed the entanglement of the MWCNTs, forming a network structure owing to the robust van der Waals forces between them. This phenomenon, known as the "reunion phenomenon" of MWCNT, is a result of their mutual attraction.[23–25] In Fig. 3(E), the SEM image indicated an oxidized in the length of MWCNT–COOH, exposing more active sites at the ends of truncated MWCNTs. This alteration provided abundant loading sites for –COOH and other functional groups.[10,21,24]

Additional support for the versatile functionality of MWCNTs is presented through energy dispersion spectroscopy (EDS) analysis (Fig. 3(D)–(F)). The EDS spectrum of MWCNT–COOH is shown in Fig. 3(F), and the primary elements and their concentrations in a specified region are detailed in the accompanying table. EDS analysis revealed the presence of carbon (C) and oxygen (O) in the MWCNT–COOH specimen. Notably, the corresponding table highlights the substantial oxygen content. These findings imply that a significant quantity of carboxyl groups (%) was introduced to the surfaces of the MWCNTs through chemical functionalization.[26]

In addition, X-ray diffraction (XRD) and X-ray photoelectron spectroscopy (XPS) analyses were performed to analyze the MWCNTs and MWCNT–COOH more precisely.

The XRD patterns of the pristine and functionalized MWCNTs are shown in Fig. 4(A). A prominent diffraction peak

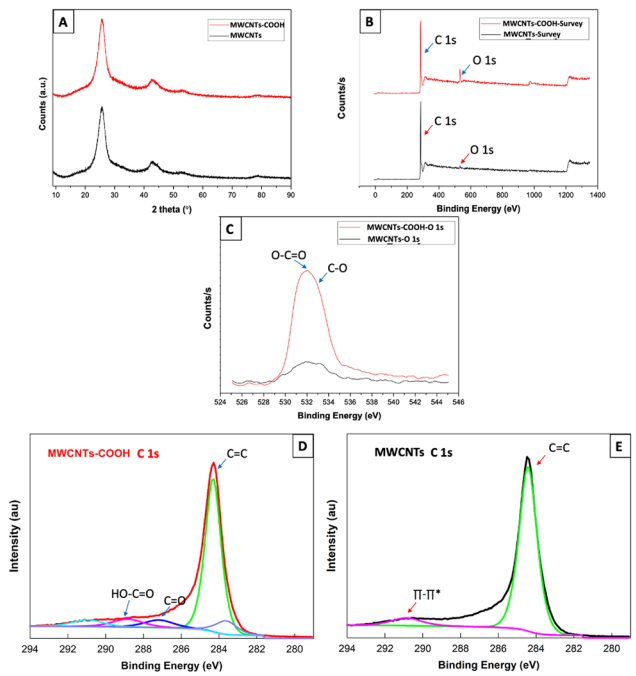

Fig. 4 XPS characterization of (A) MWCNTs and MWCNT–COOH, XRD analysis of (B)—(E) MWCNTs and MWCNT–COOH.

for the pristine MWCNTs is observed at a 2 theta (2θ) value of 25.8°. This 2θ peak corresponds to the (002) reflection plane, which is also known as the interlayer spacing between the adjacent graphite layers. The (002) reflection peaks were observed at the same 2θ values for both the pristine and functionalized MWCNTs.[27] Furthermore, the XRD patterns of the functionalized MWCNT samples closely resembled those of the pristine MWCNTs. From the XRD patterns, it can be inferred that the functionalized MWCNTs retained the same cylindrical wall structure and interlayer distance, even after functionalization. Therefore, the structure of the MWCNTs was preserved post-treatment, as confirmed by the XRD analysis.[28]

The XPS spectra of the pristine and functionalized MWCNTs are shown in Fig. 4(B)–(E). The survey scan (Fig. 4(B)) exhibits peaks corresponding to carbon (C 1s) and oxygen (O 1s). The graphitic sp^2 (C═C) structure of the MWCNT skeleton is 284.5 eV.[29] Furthermore, in Fig. 4(D), the peaks at 287 eV and 289 eV were assigned to carbonyl (–C═O) and carboxylic (HO–C═O) functionalities in MWCNT–COOH.[30] The XPS results were also in full agreement with the FTIR, SEM and TEM results.

The dual-crosslinked AlgMA and nanocomposite hydrogels dried by lyophilization were coated with gold and placed inside the FEGSEM chamber using a scanning electron microscope (model FEGSEM, Quanta FEG 450) at an accelerator voltage of 20 kV. The morphology of the internal structure of the hydrogels was investigated. The image was obtained by scanning the sample surface and cross section in the presence of a focused electron beam.

SEM images of the nanocomposite hydrogels, which were freeze-dried before imaging, are presented in Fig. 5. The internal structures of dual-crosslinked AlgMA and nanocomposite hydrogels prepared with different concentrations of MWCNT–COOH are presented. The electrons interact with the atoms in the samples, indicating the morphology, shape, and size of the samples. The results showed that the nanocomposite hydrogel morphology was affected by increasing the concentration of MWCNT–COOH. According to the SEM images, the samples revealed a porous structure with an interconnected network.[13,25,31] High concentration ratios of MWCNT–COOH were associated with structures with very small pore sizes. In addition, the morphology of the structure deteriorated as the MWCNT–COOH concentration increased, forming more closed porous structures. In addition, these images show that agglomerated MWCNT–COOH was formed on the surface of the 3% (w/v) nanocomposite hydrogel. This shows that the increase in MWCNT–COOH in the AlgMA hydrogel induces a great modification in the dual-crosslinked AlgMA hydrogel.

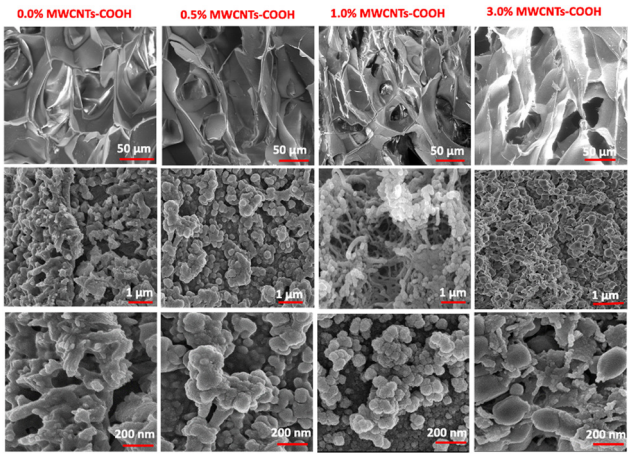

Fig. 5 SEM characterization of AlgMA and nanocomposite hydrogels.

Mechanical performance of the nanocomposite hydrogels

Uniaxial compression tests were performed in the absence and presence of carbon nanotubes to analyze the mechanical strength of AlgMA-based hydrogels designed as electroactive tissue scaffolds. The network structure containing only Alg was brittle and disintegrated at the end of the compression tests (Fig. 6(A)-left). When 1.0% w/v CNTs were added to the structure, instead of disintegrating, the pores entered each other owing to the compression process, thereby preserving the integrity of the structure (Fig. 6(A)-right). Photographs of the gels before and after the compression tests clearly show that the incorporation of MWCNT–COOH into AlgMA improves the compressive stress of the AlgMA/MWCNT–COOH hybrid hydrogels.

To examine the compression tests quantitatively, Young's Modulus E, maximum force, and deformation values that would disrupt the structural integrity of the gels were determined using the stress–strain curves of the cylindrical gel samples, as shown in Fig. 7(A). According to the bar graphs where the results are given and Young's modulus values that give the initial slope of the curves, compared with the control (AlgMA), the addition of modified MWCNTs significantly increased the mechanical stiffness. Young's Modulus of AlgMA gel was determined to be approximately 560 kPa, whereas that of AlgMA with MWCNT–COOH hydrogels at different concentrations (0.5% w/v, 1.0% w/v, and 3.0% w/v) was found to be ~800 kPa, 1280 kPa and 360 kPa, respectively. For example, the compressive modulus of a native heart is ~430 kPa. The results were compared to those of cardiac tissues, called electroactive tissues, in terms of their mechanical properties. The compressive moduli of the AlgMA and nanocomposite hydrogels were

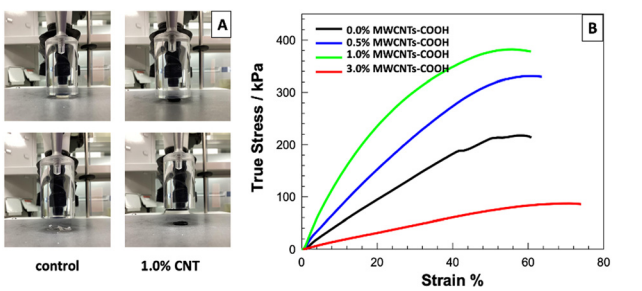

Fig. 6 Compression tests of AlgMA and nanocomposite hydrogels. (A) Photographs of the gels with and without CNT (1.0% w/v) before and after compression. (B) Typical stress–strain curve of the measurements.

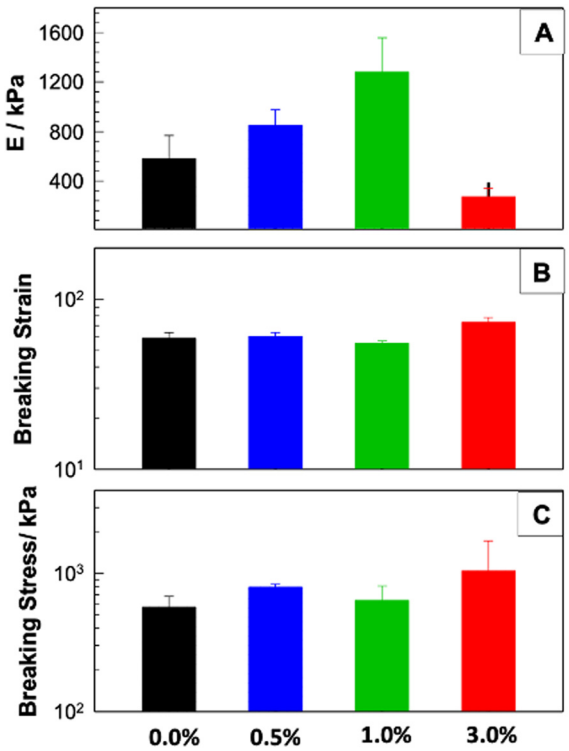

Fig. 7 Young's modulus E, breaking strain λ_f, and breaking stress σ_f as a function of MWCNT–COOH content in the structure.

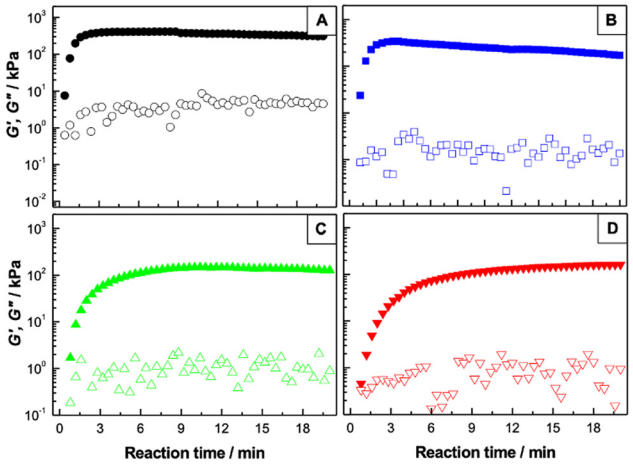

Fig. 8 Variation in elastic modulus (G', filled symbols) and viscous modulus (G'', empty symbols) values depending on the reaction time. Control gels without (●) and with different MWCNT–COOH particle concentrations are given as 0.5% (■), 1.0% (▲), and 3.0% (▼), respectively.

higher than that of the native heart. Interestingly, when the amount of MWCNTs was increased to 3.0% w/v, the modulus values decreased and were even lower than those of AlgMA hydrogels. This can be attributed to the fact that, as the amount of MWCNT increased, the particles came together and agglomerated and were not distributed homogeneously within the structure. While determining the breaking strain (λ_f) and stress (σ_f) values in Fig. 7(B) and (C), the transition from nominal values to true values is made, and the equation $\sigma_{true} = \lambda\sigma_{nom}$ is used as a function of the strain rate (λ).[32] As given, no change in λ_f and σ_f values was observed in relation to MWCNT–COOH concentration. Multi-network nanocomposite hydrogels exhibit improved mechanical properties because nanotubes, which interact with polymers, act as reinforcements. Here, modified MWCNTs may interact electrostatically with AlgMA.[33–35] While MWCNT–COOH support electrical conductivity, they also significantly increased the mechanical strength.[36] As a result of compression tests, it was determined that nanocomposite hybrid gels containing 1.0% w/v nanoparticles had the best mechanical strength.

Real-time *in situ* rheology measurements of the nanocomposite hydrogels were shown in Fig. 8. The photocrosslinking of AlgMA and nanocomposite solutions was monitored *in situ* using a rheometer. In this direction, as in the gel synthesis procedure applied to PDMS molds, polymer and initiator solutions prepared in DPBS were transferred to rheometer plates, and the change in modulus (G' and G'') under visible light irradiation was recorded (Fig. 8). As soon as the light was turned on, the $G' > G''$ state was reached, indicating that gelation had begun. Approximately 4 min later, the equilibrium modulus was recorded as 23 kPa. When a small amount of MWCNT–COOH particles (0.5%) was incorporated into the system, a slight peak was observed in the gelation kinetics, but as the number of particles increased, this peak disappeared. When the equilibrium modulus values were compared, a rapid decrease from 23 to 10 kPa was observed in gels containing 0.5% particles. The equilibrium modulus values reached after 20 min of monitoring depending on the concentration were 10, 40, and 25 kPa for 0.5, 1.0, and 3.0% MWCNT–COOH, respectively. In addition, the shear modulus of the normal myocardium was 6 kPa and the infarcted myocardium was 18 kPa.[37,38] One striking point in the gelation graphs is that the formation rate of the polymer network structure decreased with the inclusion of MWCNT–COOH particles in the structure.

Compression measurements of the gels were carried out after the addition of Ca^{2+} ions, that is after double crosslinking. It was determined that the elastic modulus, G', and Young's modulus, E, obtained before binding with Ca^{2+} had a similar behavior, increasing with the amount of MWCNT–COOH and having the highest values in the system containing 1.0% w/v MWCNT–COOH. This can be explained by the fact that the first crosslinking step, which forms hydrogels, is decisive in terms of mechanical strength.

Physical properties of the nanocomposite hydrogels

Swelling studies. The physical properties of the nanocomposite hydrogels were evaluated by swelling and degradation studies.

The *in vitro* swelling abilities of the nanocomposite hydrogels were tested at 37 °C. All hydrogels shown in Fig. 9(A) exhibited rapid swelling ability. They reached the equilibrium stage within 8 h. The prepared nanocomposite hydrogels, 0.5% and 1% (w/v) MWCNT–COOH, displayed good swelling abilities, with a swelling ratio higher than that of the control

AlgMA. The presence of different amounts of MWCNT–COOH with carboxylic hydrophilic groups increased the hydrophilicity and surface area of the prepared hydrogel to enhance the swelling capacity. Increasing the nanotube concentrations from 0.5% to 3.0% (w/v) reduced the swelling ratio. MWCNT–COOH can act as a physical crosslinker in nanocomposite hydrogels. Additionally, as higher concentrations are reached, the inhomogeneous distribution of particles within the structure may prevent water absorption by the 3.0% (w/v) MWCNT–COOH. By increasing water retention through enhanced interactions within the system and *via* hydrogen bonding, heightened concentrations resulted in reduced swelling, which was attributed to increased crosslinks, diminished pore size, and restricted water adsorption. Despite fluctuations in swelling relative to carboxyl-MWCNT concentration, all hydrogel scaffolds retained hydrophilicity, indicating their potential efficacy in retaining bodily fluids and providing nutrients to cells while upholding mechanical strength.[39,40] Especially, dual-crosslinked nanocomposite hydrogels can maintain a physiologically moist microenvironment for electroactive tissue engineering.

Degradation studies. To demonstrate the biodegradability of the prepared nanocomposite hydrogels, *in vitro* degradation was performed in DPBS for more than three weeks. The degradation (%) of the prepared conductive nanocomposite hydrogels over time was determined as a measure of the mass loss (Fig. 9(B)). These findings indicate that incorporating MWCNT–COOH into AlgMA reduces the degradation percentage over a specified duration. Within the initial 24 h, the AlgMA hydrogel experienced nearly 40% weight loss, whereas the nanocomposite hydrogels with MWCNT–COOH exhibited losses ranging from 30% to 20%, with this decreasing trend persisting until the 21st day. This clearly demonstrates the enhanced biodegradability of nanocomposite hydrogels. Evidently, the inclusion of MWCNT–COOH strengthened the stability of the nanocomposite hydrogels.

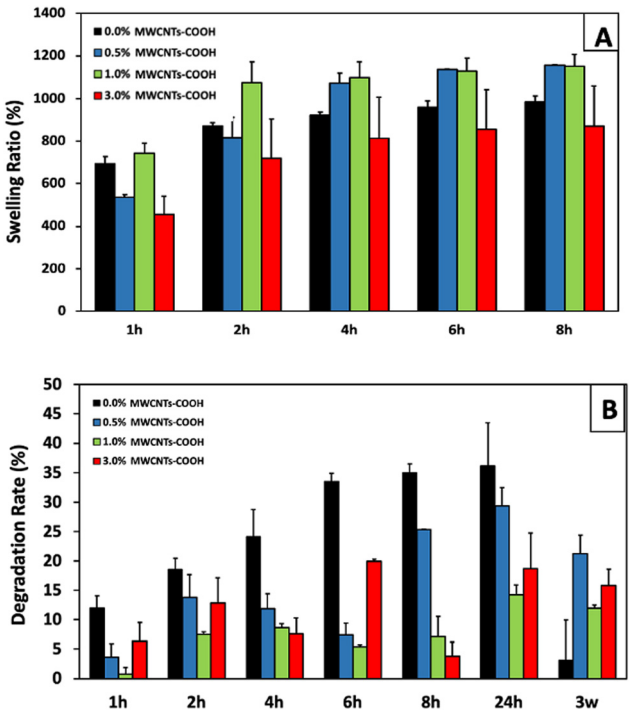

Fig. 9 Swelling (A) and degradation (B) rates (%) of the prepared nanocomposite hydrogels (A) and (B) over time.

Impedance measurements of the nanocomposite hydrogels

Electrochemical impedance spectroscopy was used to evaluate the electron transfer properties of the developed electrodes. As a result of these measurements, the R_{ct} (charge transfer resistance, which is the opposite of electron movement) values of the electrodes can be calculated.[41]

As shown in Fig. 10, the largest semicircle diameter was obtained for the bare GC electrode and R_{ct} was 35.064 Ω. The diameter of the semicircle obtained for the control GC/AlgMA working electrode was larger than that of the bare GC electrode, and its R_{ct} was 2563.7 Ω. On the other hand, the R_{ct} value was quite small for the GC/3.0% w/v nanocomposite hydrogel electrode. Based on these results, the electrical conductivity increased with decreasing impedance measurements. In addition, the electrical properties were also improved in the nanocomposite hydrogels, with the 3.0% MWCNT–COOH hydrogel being the most conductive (465.99 Ω) and the 0.5% w/v MWCNT–COOH hydrogel being the least conductive (1714.5 Ω) of the MWCNT–COOH hydrogels. At lower frequencies, which are more physiologically relevant, the impedance of GC/AlgMA/CNTs–COOH was significantly lower than that of pristine AlgMA hydrogels. Previous reports have shown that conductive scaffolds are superior to their more insulating polymer counterparts for improved electrical signal propagation among electroactive cells.[6] Therefore, we anticipate that nanocomposite hydrogels, which are not only more electrically conductive but also mechanically stronger than AlgMA hydrogels, are promising new scaffold materials for electroactive tissue engineering.

In vitro cell viability and proliferation studies of nanocomposite hydrogels

Morphological images of fibroblasts after 168 h are shown in Fig. 11. Although the fibroblast cells used as the control group showed increased proliferation over time, the viability and proliferation tendencies of the cells on the material differed.

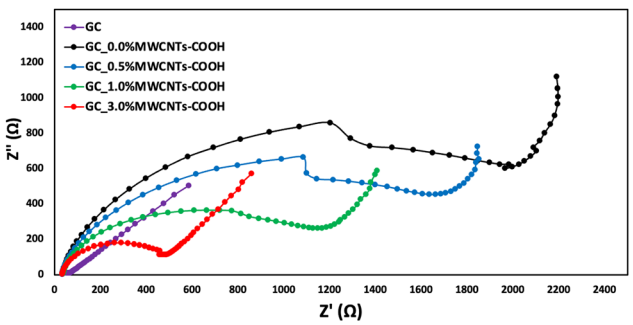

Fig. 10 Electrical conductivities of prepared AlgMA and nanocomposite hydrogels.

Surface modification has been used for the functionalization of carbon-based nanomaterials. Functionalizing surfaces affect cytotoxicity. Our cell studies with fibroblasts indicate the importance of the surface area of MWCNT–COOHs as well as the toxicity of dispersed carbon nanomaterials. Studies have shown that CNTs have toxic effects depending on time and dose.[13,14,42] In our study, we showed that the toxic effect varied depending on the time and MWCNT–COOH concentration. Studies have shown that CNTs have toxic effects depending on time and dose. In our study, we showed that the toxic effect varied depending on the time and MWCNT–COOH concentration. Day-dependent viability and proliferation of fibroblasts cultured on 0.5% and 1.0% (w/v) nanocomposite hydrogels were observed to be similar to the fibroblasts cultured alone in the control group (for 72 h), while the cells in the 0.5% MWCNT–COOH group showed the best viability and proliferation compared to the fibroblasts cultured alone for 72 h (>70% cell viability). However, in the long term (168 h), the highest viability was observed for the 3.0% MWCNT–COOH group among the different MWCNT–COOH coated surfaces (Fig. 11, >70% cell viability, $p < 0.05$). Moreover, they found that the incorporation of different concentrations of MWCNT–COOH into AlgMA hydrogels promoted cell alignment and improved cell function. It has been hypothesized that nanocomposite hydrogels, such as those loaded with carbon nanotubes (CNTs), promote cell recruitment and migration more effectively than unloaded hydrogels. Cell migration and recruitment studies confirmed that small concentrations of CNTs significantly enhanced cell migration within the hydrogels. Electroactive polymers can stimulate cells in the context of tissue engineering by providing electrical current. Therefore, in our study, electrical stimulation affected the growth of cells.[43]

SEM analysis and annexin/propidium iodide staining

Cell adhesion on the surfaces was examined using SEM, as shown in Fig. 12(A). The cells adhered to and entered the materials. According to Annexin V/PI staining, live cells showed no fluorescence, early apoptotic cells showed green fluorescence, late apoptotic cells, and necrotic cells showed red fluorescence

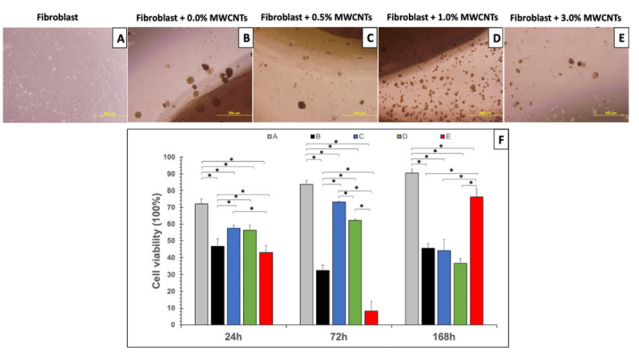

Fig. 11 (A)—(E) Photograph showing the uptake of MCNTs–COOH by cells. Fibroblast proliferation on differently coated surfaces (scale bar = 500 μm). (F) Fibroblast viability on differently coated surfaces over 168 h (*$p < 0.05$, mean ± std, $n = 3$). This is an image of cells on the seventh day.

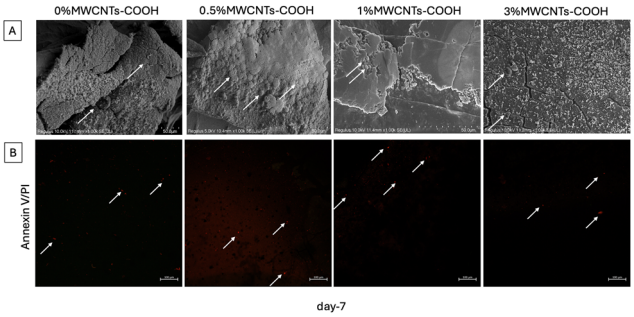

Fig. 12 Fibroblast culture on AlgMA and nanocomposite hydrogel surfaces. (A) Field emission scanning electron microscopy (FE-SEM) images of fibroblasts on AlgMA and nanocomposite hydrogel samples on day-7. Arrows indicate fibroblasts on the surface (50 μm). (B) Annexin V/PI staining of fibroblasts on AlgMA and hydrogels on day 7. The arrow shows late apoptotic/necrotic cells on the surfaces (100 μm).

(Fig. 12(B)). All surfaces were found to be suitable for fibroblast adhesion and caused apoptosis at the expected rate on day 7.

Experimental

Materials

Alginic acid sodium salt from brown algae (low-viscosity alginate), methacrylic anhydride (MA; purity ≥94%), triethanolamine (TEA; purity ≥99%), *N*-vinylcaprolactam (VC; purity ≥98%), Eosin Y, and calcium chloride dihydrate (purity ≥99%) were all purchased from Sigma-Aldrich. Dulbecco's phosphate-buffered saline (DPBS), Dulbecco's modified Eagle's medium (DMEM), fetal bovine serum (FBS), and penicillin/streptomycin, P/S were manufactured by GIBCO/Life Technologies and purchased from Thermo Fisher Scientific carbon nanotubes (outer diameter: 5–15 nm; purity: >99 wt%) were purchased from Sigma.

Synthesis of methacrylated alginate (AlgMA)

AlgMA was synthesized according to a published procedure.[17] AlgMA was synthesized by the reaction of the hydroxyl groups on pristine Alg with the vinyl groups on methacrylic anhydride. Briefly, 2.5% w/v Alg was weighed and dissolved in DI water at room temperature to obtain an Alg solution. After the complete dissolution of Alg, methacrylic anhydride (MA) was added dropwise into the Alg solution and allowed to react while stirring in a magnetic stirrer at 300 rpm for 3 days at room temperature. The pH was adjusted to 7 using 5 N NaOH. After the reaction, ethanol was added to the mixture to separate the AlgMA from the solution. After the complete precipitate was formed, the solution was filtered using ordinary filter paper and dissolved in DI water. The precipitate was then transferred to a dialysis membrane (MWCO 12–14 kDa, SERVAPOR dialysis tubing) and dialyzed against ultrapure water for five days to remove impurities (unreacted methacrylic anhydride and its salts). The solutions were then removed from the dialysis membrane, placed in glass jars, and frozen for lyophilization.

Synthesis of MWCNT–COOH

Commercial MWCNTs were functionalized with carboxylic acid groups (–COOH functional groups) using the HNO_3 oxidative method.[10] For this purpose, 200 mg of MWCNTs were dispersed in 100 mL concentrated (65%) HNO_3 by sonication in a water bath for 2 h. The mixture was then stirred with a magnetic stirrer at room temperature for 2 h. To remove the highly acidic residue, the MWCNT–COOH were washed with double-distilled water and neutralized. The resulting product was then dried overnight in an oven.

Photocrosslinking of nanocomposite hydrogels

Alg was functionalized with methacrylic anhydride (MA) to obtain photosensitive structures of AlgMA macromers. To prepare photocrosslinked AlgMA and AlgMA/MWCNT–COOH nanocomposite hydrogels, 5% (w/v) AlgMA was dissolved in DPBS at 50 °C. Functionalized MWCNTs (5 mg) were added to the AlgMA solution to obtain AlgMA-coated MWCNT–COOH. The solution was sonicated in a water bath. Subsequently, a selected amount of the prepared solution was added to a 10% (w/v) AlgMA solution, which included photo-activators prepared with triethanolamine (TEA, 1.875% (w/v)), *N*-vinylcaprolactam (VC, 1.25% (w/v)), and Eosin Y disodium salt (0.5 mM), to form a prepolymer solution for gelling. Gels were then prepared and optimized by varying the concentration of MWCNT–COOH in the solution (0.5%, 1%, and 3% (w/v)). To fabricate photocrosslinked nanocomposite multi-network hydrogels, the prepared solutions were injected into a PDMS mold to obtain the hydrogel disks. Subsequently, the solutions were photocrosslinked with visible light in the range of 420–480 nm using a VALO Visible Light Photocrosslinking device (Ultradent, USA)[38] for 240 s, resulting in the formation of hydrogels. Subsequently, 1 M Ca^{2+} ions were added to the photocrosslinked nanocomposite hydrogels for 5 min to achieve double crosslinking of nanocomposite hydrogels.

Characterization studies

The structural characterization of the prepared AlgMA, MWCNTs, MWCNT–COOH, and double-crosslinked nanocomposite hydrogels was confirmed by Fourier transform infrared (FTIR) and proton nuclear magnetic resonance spectroscopy (^{1}H NMR) analyses. A Jasco FT/IR-6700 spectrometer was used for the FTIR characterization. ^{1}H NMR (Varian UNITY INOVA instrument) was applied to both pristine Alg and AlgMA to determine chemical differences. Deuterium oxide (D_2O) was selected as the solvent for Alg and AlgMA to obtain ^{1}H NMR spectra at 25 °C, at a frequency of 500 MHz. The topography and composition of AlgMA and nanocomposite hydrogels were determined using scanning electron microscopy (SEM), ESEM-FEG (Quanta FEG 650 ESEM, FEI Inc.), and transmission electron microscopy (TEM, JEOL JEM 1220). Cross-sectional morphological images of the hydrogels were obtained using SEM.[27,38]

X-Ray diffraction (XRD, Bruker D8 Discover) analysis was applied for MWCNTs and MWCNT–COOH with parameters: Cu tube 1.5418 Å, 2θ = 5–90°, opening degree: 0.1°, time/step: 0.6 s, increment: 0.02°. In addition, X-ray photoelectron spectroscopy (XPS) analyses of the MWCNTs and MWCNT–COOH were carried out using a Thermo Scientific K-Alpha XPS instrument with Al K-alpha monochromatic radiation (1486.3 eV). For XPS measurements, the dried samples were exposed to an X-ray spot size and a 50.0 eV pass energy. The take-off angle was set to 90°. All the measured peaks were deconvoluted and fitted using Avantage 5.9 software. The C 1s peak 284.5 eV was designated for the assessment.

Mechanical properties of the nanocomposite hydrogels

The compressive strengths of the prepared nanocomposite hydrogels were examined to understand the load-bearing properties of the scaffolds. A TA.XT plus Texture Analysis mechanical tester was used for the compression testing. Compression tests were performed using 200 μL of the pre-gel solution. For the compressive experiments, dual-crosslinked nanocomposite hydrogels were prepared as described previously. The prepared crosslinked hydrogels were then placed on a testing device. Compression tests were carried out at a strain rate of 0.6 mm min^{-1} until reaching the failure point (Max strain of 98%). The Young's modulus obtained from the compression tests was calculated from the slope of the stress–strain curves within the deformation range of 5–15%, corresponding to the linear region. At least five samples were tested for each time condition and the average values were calculated.

Real-time *in situ* rheology of the nanocomposite hydrogels

Photocrosslinking reactions and rheology were performed using an Anton Paar Physica MCR 102 rheometer with a photocuring quartz bottom plate unit attached to the rheometer. An Omnicure S2000 lamp source, which emits radiation from the quartz plate, was used with a 320–500 nm bandpass filter. All photocrosslinking experiments were performed for 20 min, and a steel upper parallel plate with a diameter of 15 mm was employed. For all reported analyses, an initial gap size of 0.5 mm was used. To observe the gelation kinetics of the methacrylated alginate hydrogels, liquid samples were transferred between the plates of the rheometer immediately after mixing (time t = 0), and the storage moduli G' and loss moduli G'' were monitored as a function of time at a frequency of 1 Hz and a strain of 0.1% under light irradiation at 24 °C.

Physical properties of the nanocomposite hydrogels

The swelling behavior of AlgMA and nanocomposite hydrogels in DPBS was investigated using the same preparation method as that used for mechanical testing. The dual-crosslinked nanocomposite hydrogels were prepared and frozen. Frozen nanocomposite hydrogels were lyophilized, weighed, and recorded to calculate swelling ratios. The weighed samples were incubated in DPBS for 1, 2, 4, 6, or 8 h at 37 °C to reach the equilibrium swelling state. The hydrogel disks were removed from PBS, and the weights of the swollen (W_s) hydrogel sample were measured. The swelling ratio was calculated using eqn (1) for each material (n = 4).[38]

$$\text{Swelling (\%)} = (W_s - W_i)/W_i \times 100 \quad (1)$$

W_s = swollen weight, W_i = initial weight before swelling.

The degradation studies were performed in the same manner as the swelling experiments. Lyophilized materials were weighed and incubated in a collagenase type II solution in PBS for up to 3 weeks at 37 °C. Collagenase (10 mg mL^{-1}) was added to the medium to monitor enzymatic degradation. At predetermined time points, excess PBS was removed and the samples were frozen and lyophilized. The lyophilized nanocomposite hydrogels were weighed and recorded. The percentage mass loss was calculated using eqn (2) ($n = 4$).[38]

$$\text{Weight loss (\%)} = (W_i - W_d)/W_i \times 100 \quad (2)$$

W_d = final dried weight, W_i = dried weight before degradation.

Impedance measurements of nanocomposite hydrogels

Conductivity measurements were performed on the working electrodes, bare GC, AlgMA, and the prepared nanocomposite hydrogels (AlgMA/MWCNT–COOH). Potentiostat electrochemical impedance spectroscopy (EIS) was performed in 0.10 mol L^{-1} KCl, 0.10 mol L^{-1} HCl and 5.0 mmol L^{-1} [Fe (CN)6]3-/4-solution media; the frequency range was 10–0.1 MHz, and points/decade 10 mV. Impedance at each frequency was recorded.[41]

In vitro cell studies of the nanocomposite hydrogels

Human dermal fibroblasts (ATCC) were cultured in DMEM-LG (Gibco) supplemented with 10% FBS (BioWest), 1% Pen-Strep, and L-glutamine (Sigma-Aldrich) at 37 °C in a humidified incubator (5% CO_2) for 7 days. The medium was changed twice per week. At 80–85% confluence, the cells were trypsinized with TrypLE solution (Gibco), and cell viability was assessed by trypan blue dye exclusion. Cell viability/proliferation was tested using WST-1.[16] For this purpose, fibroblasts (50 000 cells per mL) were seeded on nanocarbon-based materials and controls (fibroblasts alone and AlgMA) for 168 h. After 24, 72, and 168 h of incubation, cell metabolic activity was assessed using a water-soluble tetrazolium-based assay (10% WST-1, 4-[3-(4-iodophenyl)-2-(4-nitrophenyl)-2*H*-5-tetrazolio]-1,3-benzene disulfonate) for 2 h. 100 μL of medium for each condition was transferred into ELISA microplates (96-well plates, Corning Life Sciences, Lowell, MA, USA) for spectrophotometric measurement. The absorbance of the solution was measured spectrophotometrically at 450 nm (Tecan). Data were expressed as (O.D. value of the sample − O.D. value of the blank) × 100/O.D. value of the sample. All analyses were performed in triplicates.

SEM analysis and annexin/propidium iodide staining. Fibroblasts on AlgMA and nanocomposite hydrogel surfaces were evaluated by scanning electron microscopy (SEM) on the 7th day of culture. For this purpose, media was drawn from the wells, and the cells were washed once with PBS. After washing, the cells were fixed in 3.7% formaldehyde (0.5 mL) at 37 °C for 20 min. The surface of the material was analyzed using SEM (FEI Quanta 200F). FITC Annexin V and propidium iodide (PI) were used following the manufacturer's instructions (Invitrogen) for apoptosis/necrosis detection after seven days of culture.

Data analysis

Data analysis was performed using a *t*-test. Error bars represent the mean ± standard deviation (SD) of measurements (*$P < 0.05$, **$P < 0.01$, ***$P < 0.001$, and ****$P < 0.0001$).

Conclusions

The utilization of electroactive scaffold structures is becoming more prevalent in mimicking the microenvironment of electroactive tissues, such as the heart and nerves. In this study, multinetwork hydrogels were fabricated using physical–chemical crosslinking methods and hydrogen bonding. Our results clearly showed that at lower frequencies, which are more physiologically relevant, the impedance of the nanocomposite hydrogels was significantly lower than that of pristine AlgMA hydrogels. *In vitro* cell studies showed enhanced fibroblast adhesion and proliferation on nanocomposite hydrogels compared to AlgMA. MWCNT–COOH can be employed to encourage cell proliferation while maintaining chemical stability, mechanical properties, and biocompatibility in electroactive tissue engineering. The incorporation of modified MWCNTs into AlgMA not only increased the electrical conductivity but also facilitated the creation of mechanically robust biomimetic and biocompatible hydrogels. The results of all experiments were consistent. Nanocomposite hydrogels with 1% w/v MWCNT–COOH exhibited better material properties than hydrogels with other concentrations. Therefore, we anticipate that nanocomposite hydrogels, which are not only more electrically conductive, but also mechanically stronger than AlgMA hydrogels, are promising new scaffold materials for electroactive tissue engineering.

Author contributions

R. T. contributed to project ideas and design. R. T., D. C. T. and B. Ç. S. conducted the experiments and characterization. R. T. structured and drafted the manuscript. R. T., B. Ç. S. and D. C. T provided comments and feedback to improve the manuscript writing.

Data availability

The data supporting this article are provided within the article.

Conflicts of interest

The authors declare no competing financial interests.

Acknowledgements

This study was financially supported by the Scientific Research Projects Committee of Istanbul University-Cerrahpaşa (BAP, FBA-2021-35559), Istanbul, Turkey. D. C. T. thanks the Turkish Academy of Sciences (TUBA) for partial support. We would like to thank Dr Şener Sağlam for his contribution.

Notes and references

1 N. Bursac, Y. H. Loo, K. Leong and L. Tung, *Biochem. Biophys. Res. Commun.*, 2007, **361**, 847–853.
2 T. Dvir, B. P. Timko, M. D. Brigham, S. R. Naik, S. S. Karajanagi, O. Levy, H. Jin, K. K. Parker, R. Langer and D. S. Kohane, *Nat. Nanotechnol.*, 2011, **6**, 720–725.
3 M. E. Valentine, B. D. Kirby, T. R. Withers, S. L. Johnson, T. E. Long, Y. Hao, J. S. Lam, R. M. Niles and H. D. Yu, *Microb. Biotechnol.*, 2020, **13**, 162–175.
4 O. Jeon, C. Powell, S. M. Ahmed and E. Alsberg, *Tissue Eng., Part A*, 2020, **16**, 2915–2925.
5 A. I. Chou and S. B. Nicoll, *J. Biomed. Mater. Res., Part A*, 2009, **91**, 187–194.
6 M. Mehrali, A. Thakur, C. P. Pennisi, S. Talebian, A. Arpanaei, M. Nikkhah and A. Dolatshahi-Pirouz, *Adv. Mater.*, 2017, **29**, 1603612–1603637.
7 S. J. Malode, S. Pandiaraj, A. Alodhayb and N. P. Shetti, *ACS Appl. Bio Mater.*, 2024, DOI: **10.1021/acsabm.3c00983**.
8 E. W. Wong, P. E. Sheehan and C. M. Lieber, *Science*, 1997, **277**, 1971–1975.
9 W. Zhang, Z. Zhang and Y. J. Zhang, *Nanoscale Res. Lett.*, 2011, **6**(1), 555.
10 S. Sahebian, S. M. Zebarjad, J. V. Khaki and A. Lazzeri, *Nanostruct Chem.*, 2015, **5**, 287–293.
11 S. R. Shin, S. M. Jung, M. Zalabany, K. Kim, P. Zorlutuna, S. Kim, M. Nikkhah, M. Khabiry, M. Azize, J. Kong, K. Wan, T. Palacios, M. R. Dokmeci, H. Bae, X. Tang and A. Khademhosseini, *ACS Nano*, 2013, **7**(3), 2369–2380.
12 W. Zheng, Y. Li, L. Xu, Y. Huang, Z. Jiang and B. Li, *Polymer*, 2020, **211**, 123095.
13 J. Zhang, L. Zeng, Z. Qiao, J. Wang, X. Jiang, Y. S. Zhang and H. Yang, *ACS Appl. Mater. Interfaces*, 2020, **12**(27), 30247–30258.
14 G. Chen, Y. Guo, S. B. Hsiao, K. Hou and M. Zhu, *Sci. China: Technol. Sci.*, 2022, **65**, 1160–1168.
15 E. Gómez-Ordóñez and P. Rupérez, *Food Hydrocolloids*, 2011, **25**, 1514–1520.
16 J. A. Burdick, C. Chung, X. Jia, M. A. Randolph and R. Langer, *Biomacromolecules*, 2005, **6**, 386–391.
17 M. Tavafoghi, A. Sheikhi, R. Tutar, J. Jahangiry, A. Baidya, R. Haghniaz and A. Khademhosseini, *Adv. Healthcare Mater.*, 2020, **9**, 1901722.
18 Y. Lin, A. M. Rao, B. Sadanadan, E. A. Kenik and Y. P. Sun, *J. Phys. Chem. B*, 2002, **106**, 1294–1298.
19 G. Qu, J. Zhou, S. Liang, Y. Li, P. Ning, K. Pan, W. Ji and H. Tang, *Mater. Chem. Phys.*, 2022, **278**, 125688.
20 L. Jiang, H. Yu, X. Zhou, X. Hou, Z. Zou, S. Li, C. Li and X. Yao, *Desalination Water Treat*, 2016, **57**, 18446–18462.
21 M. D. Ellison and P. J. Gasda, *J. Phys. Chem. C*, 2008, **112**, 738–740.
22 T. Alizadeh, F. Zargar and M. R. Zamanloo, *J. Mater. Sci.: Mater. Electron.*, 2019, **30**, 7981–7991.
23 Y. Wu, H. Cao, M. Duan, E. Li, H. Wang, Z. Yang, D. Wang and W. He, *Liq. Cryst.*, 2018, **42**, 1023–1031.
24 J. Y. Gu, L. Zhang and X. K. Jiang, *Adv. Mater. Res.*, 2011, 805–809.
25 Y. Wu, H. Cao, M. Duan, E. Li, H. Wang, Z. Yang, D. Wang and W. He, *Liq. Cryst.*, 2018, **45**, 1023–1031.
26 Z. Zhao, Z. Yang, Y. Hu, J. Li and X. Fan, *Appl. Surf. Sci.*, 2013, **276**, 476–481.
27 G. W. Lee, J. Kim, J. Yoon, J. S. Bae, B. C. Shin, I. S. Kim, W. Oh and M. Ree, *Thin Solid Films*, 2008, **516**, 5781–5784.
28 F. Y. Wu and H. M. Cheng, *J. Phys. D: Appl. Phys.*, 2005, **38**, 4302–4307.
29 O. Akhavan, R. Azimirad, S. Safa and M. M. Larijani, *J. Mater. Chem.*, 2010, **20**, 7386.
30 H. M. Joseph, S. Sugunan, L. Gurrala, M. K. Mohan and S. Gopi, *Ceram. Int.*, 2019, **45**(12), 14490–14499.
31 A. M. K. Esawi, K. Morsi, A. Sayed, M. Taher and S. Lanka, *Composites, Part A*, 2011, **42**, 234–243.
32 H. Kılıç, D. C. Tuncaboylu, A. Argun and D. Civelek-Öztürk, *ACS Appl. Polym. Mater.*, 2022, **4**(3), 1717–1727.
33 K. Mitamura, T. Imae, N. Saito and O. Takai, *J. Phys. Chem. B*, 2007, **111**(30), 8891–8898.
34 S. C. Tjong, *Mater. Sci. Eng., R*, 2006, **53**(3), 73–197.
35 A. C. Balazs, T. Emrick and T. P. Russell, *Science*, 2006, **314**(5802), 1107–1110.
36 V. Martinelli, G. Cellot, A. Fabbro, S. Bosi, L. Mestroni and L. Ballerini, *Front. Physiol.*, 2013, 4.
37 B. Peña, S. Bosi, B. A. Aguado, D. Borin, N. L. Farnsworth, E. Dobrinskikh, T. J. Rowland, V. Martinelli, M. Jeong, M. R. G. Long Taylor, C. S. R. Shandas, O. Sbaizero, M. Prato, K. S. Anseth, D. Park and L. Mestroni, *ACS Appl. Mater. Interfaces*, 2017, **9**(37), 31645–31656.
38 R. Tutar, S. Y. Koken, D. C. Tuncaboylu, B. Çelebi-Saltik and C. Ozeroglu, *New J. Chem.*, 2023, **47**, 10759–10769.
39 S. M. Haung, Y. T. Lin, S. M. Liu, J. C. Chen and W. C. Chen, *Gels*, 2021, **7**, 165.
40 S. Kaviani, A. Talebi, S. Labbaf and F. Karimzadeh, *Int. J. Biol. Macromol.*, 2024, **259**, 129276.
41 P. E. Randviir and E. C. Banks, *Anal. Methods*, 2013, **5**(5), 1098–1115.
42 A. Patlolla, B. Knighten and P. Tchounwou, *Ethn. Dis.*, 2010, **20**, 65–72.
43 H. Ravanbakhsh, G. Bao and L. Mongeau, *Sci. Rep.*, 2020, **10**, 2543.